Models of the Penetration of Sunlight into the Atmosphere of Titan

M. G. Tomasko,[1] M. Lemmon,[1] L. R. Doose,[1] P. H. Smith,[1], A. Eibl[1] & R. A. West[2]

[1]*Lunar and Planetary Laboratory, University of Arizona, Tucson, AZ 85721, USA*
E-mail: mtomasko@lpl.arizona.edu Fax: +1 520 621-2994
[2]*Jet Propulsion Laboratory, 4800 Oak Grove Drive, Pasadena, CA 91109, USA*

During the development of Huygens' optical instruments for the descent into Titan's atmosphere, models of sunlight penetration into the atmosphere were required to guide the sensitivity, dynamic range, wavelength range and geometric fields of view of the instruments. This paper summarises two basic models that were developed to support the design of the Descent Imager/Spectral Radiometer (DISR) instrument. The first model assumes spherical particle shape, and the second includes 'fractal' particles produced by cluster-cluster aggregation in an attempt to reproduce both the observed strong forward-scattering and high polarisation near 90° scattering angles. Both models use a paramaterised mass production function at high altitudes, coagulation of particles to larger sizes, and sedimentation out of the atmosphere. Free parameters include the mass production rate, the electrical charge on the particles that inhibits growth to large size, and the altitude below which 'rainout' is assumed to remove particles. The real and imaginary refractive indices of the photochemically-produced small haze particles are taken from Khare et al. (1984) with only minor adjustments. The ground albedo is adjusted to agree with the observed albedo at continuum wavelengths in the red and near-IR. Gaseous absorption by methane longward of 1 μm is treated by an exponential-sum method based on extrapolation to conditions on Titan of absorption band models constrained by the observations of Giver et al. (1990) at long paths and low temperatures. Shortward of 1 μm, absorption by methane at low temperatures is treated following Karkoschka (1990). We describe the wavelength- and altitude-dependent parameters used for both models, show their ability to reproduce a wide variety of observational constraints, and indicate the downward direct, downward diffuse and upward fluxes of sunlight as functions of altitude throughout Titan's atmosphere for both models.

1. Introduction

In order to define the properties of optical instruments for operation in Titan's atmosphere, it is necessary to estimate the intensity of sunlight inside the atmosphere as a function of altitude, direction and wavelength. Several observational constraints are available that serve to limit the range of such estimates. These include the variation of geometric albedo in the visible and near-IR, as well as photometry and polarimetry of Titan at a large range of phase angles during the Pioneer and Voyager missions. When work began on the Huygens mission, the available models emphasised the intensity and polarisation of sunlight reflected from the atmosphere, rather than the internal radiation field. These models included those of Rages and Pollack (1980),

aimed at reproducing the geometric albedo and the wavelength dependence of the variation of brightness of the integrated disc at small phase angles, the models of Toon et al. (1980), which included cloud microphysics, and our own models of the variations of brightness, linear polarisation, and limb darkening at large phase (Tomasko & Smith, 1982; Tomasko et al., 1989). All of these models used spherical particles and were limited to the region shortward of about 1 μm wavelength.

This paper briefly describes two models of the solar radiation field inside Titan's atmosphere that were developed at the University of Arizona since the beginning of our work on the Huygens mission. Both included extensions to include the wavelength region 1-2 μm using extrapolations of band models fitted to the low temperature measurements of the absorption of gaseous methane by Giver (1990) as well as cloud microphysics to guide the variation of particle properties with height.

The first model (dating from 1989) assumed spherical particles, and suffers from what has become the classic difficulty of reproducing both the high brightness of Titan observed at forward-scattering angles and the high degree of linear polarisation observed near 90° scattering. The more recent second model (Lemmon, 1994) includes an irregular particle shape resulting from aggregation of clusters of very small spherical particles following a method described by West (1990). Comparison of the different variations of solar flux with depth into the atmosphere by these two models, which both agree with the external albedo spectrum, provides a rough measure of the uncertainty of the penetration of solar radiation to deep levels in Titan's atmosphere.

In the next section, we describe the approach used for both models and indicate their ability to reproduce the available optical observations of Titan. Section 3 gives the solar fluxes computed for each model as functions of wavelength and altitude.

2. Physical Models

2.1 Background

Calculations of the intensity of sunlight inside Titan's atmosphere require a large amount of information about both the particles and gases in the atmosphere. Functions are needed to describe the number density, real and imaginary refractive index, and the size and shape of the haze particles throughout the atmosphere, with similar information for any condensation clouds in the troposphere. The variation of surface reflectivity with wavelength is also needed. In addition, the mixing ratio profile of methane and any other absorbing gases, as well as the wavelength dependence of their absorption coefficients at the appropriate low temperatures and long paths, are also needed.

This relatively large number of functions can be constrained by relatively few optical measurements, including the observed geometric albedo versus wavelength, and the brightness and polarisation at the few observed wavelengths as functions of phase angle available from space missions, or at many wavelengths over the few degrees of phase angle observable from the Earth. Unless other physical constraints can be applied to limit the range of the optical parameters of the haze and cloud particles with depth into the atmosphere, the prospects of tightly constraining models of sunlight penetration into Titan's atmosphere are poor.

It is for this reason that considerable effort has been devoted to including additional physical processes in models of the distribution and properties of haze and cloud particles in Titan's atmosphere. For example, if the processes of coagulation to larger particle size and sedimentation out of the atmosphere are included, and the number density and optical properties of particles at each altitude are assumed to be in steady state, then the functions describing the variation of particle size and scattering properties with depth can be replaced with a few constants such as the mass production rate of aerosol material, the height at which particles are produced, and the electrical charge on the particles, which acts to inhibit coagulation. If a particle shape is

assumed, then the variation of scattering properties with altitude can be computed in steady state, and the relatively few optical observations can be used much more effectively to constrain the range of models.

2.2 Stratospheric haze properties

The approach used in our models for specifying the properties of haze particles was as follows. Both models assume that small spherical haze particles are produced photochemically from the gas at high altitudes at a parameterised mass production rate, *MPR* g/cm^2. Both models relate the variation of particle size with depth into the atmosphere by including sedimentation and coagulation to larger sizes in the presence of a small electrical change, Q per unit particle radius, which controls the rate of this process. The relationship between particle size and sedimentation rate is different for the spherical particles and for the fractal aggregrates because of the different aerodynamic drag in view of the different effective densities of the two types of particles (see Lemmon, 1994). The two constants *MPR* and Q determine the total mass loading of the photochemical haze as well as the variation of particle size with depth into the atmosphere. Both models require removal of the photochemical haze below some altitude, Z, between the lower stratosphere and the surface (possibly by rainout) in order to reproduce the shapes of weak methane bands that are formed at deep atmospheric levels.

The refractive indices of the haze particles are taken to be essentially those values measured for tholin particles by Khare et al. (1984). The real refractive index is taken directly from these authors. The imaginary index is allowed to vary slightly from the measured values (4/3 times the measured values for the fractal aggregrate model and a value generally within 20% of the measured value for the spherical model) as shown in Fig. 1.

2.3 Condensation clouds

At still deeper levels, condensation clouds are included in the troposphere. These clouds are assumed to consist of particles sufficiently large so that their optical

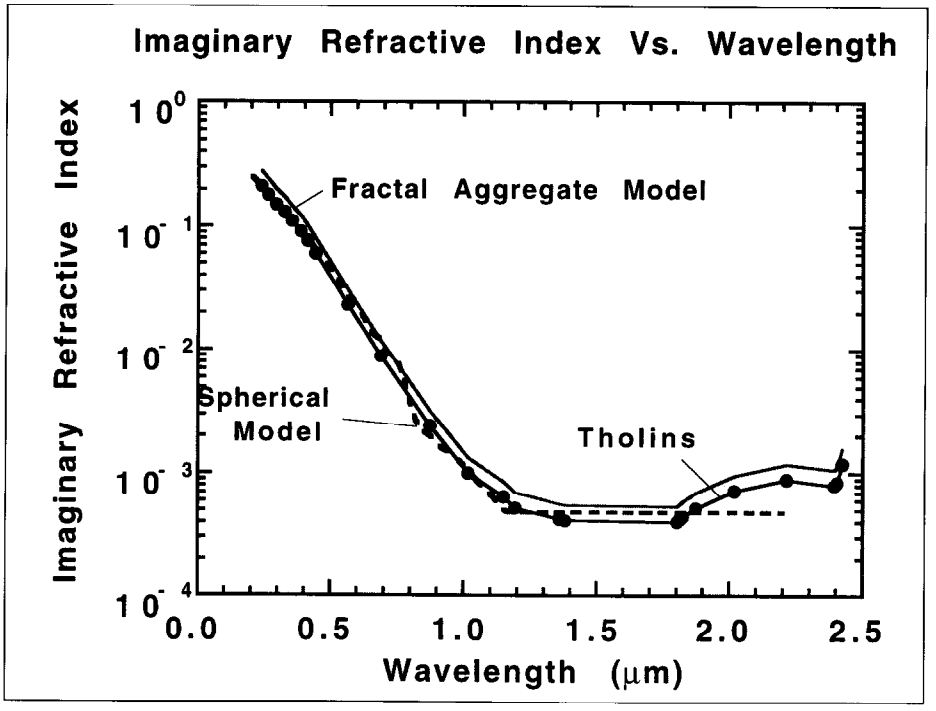

Fig. 1. Imaginary index of refraction used for the models consisting of spherical particles and the models using aggregate particles. Also shown are the data from Khare et al. (1984). The line representing the values for the fractal model is 4/3 times the tholin values.

properties are independent of wavelength shortward of 2.2 μm. The optical depth of such condensation clouds is constrained by measurements of the geometric albedo of the integrated disc to be small ($\leq$ a few tenths) averaged over the disc. It is possible that these clouds are, in fact, optically thick in small areas and essentially absent over most of the disc. The vertical locations of these particles are not well constrained by available observations made from outside the atmosphere. In our older model based on spherical particles, condensation clouds were placed in two layers: in the lower stratosphere (near 55 km) where they may consist of molecular species photochemically produced at higher altitudes that diffuse down to regions where the temperature is sufficiently low for condensation (see Sagan and Thompson, 1984); and in the troposphere, where they may consist of condensed methane. In our more recent fractal models, we uniformly distributed a wavelength-independent optical depth of 0.46 below the rainout altitude of 88 km. Because the location and thickness of these clouds is not well constrained by the existing observations from outside the atmosphere, we simply assumed the phase function of these particles to be a 2-term Henyey-Greenstein function with the parameters indicated in Table 1 for both of our models. The single-scattering albedo of these particles was assumed to be unity in both models.

2.4 Methane absorption

In both models, the observed depths of methane bands of different strengths provide important constraints for determining the model parameters and hence the penetration of sunlight to deep levels in Titan's atmosphere. We used the low temperature measurements by Giver et al. (1990) as fitted by Malkmus band models to extrapolate the transmission in small spectral intervals to the path lengths for Titan. These transmissions were then fitted by an exponential sum technique so that they could be used in our scattering models. In each wavelength region beyond 1 μm where methane absorption occurs, we approximated the transmission as a function of path length by an 8-term sum of exponential terms with different fitted absorption coefficients. The weights of each of the eight terms were the weights for 8-point Gaussian quadrature, and the eight absorption coefficients were obtained by fitting the band model expressions derived from the laboratory observations following Asano & Uchiyama (1987).

Shortward of 1 μm, laboratory measurements of the absorption coefficients of methane at the appropriate long paths and low temperatures are generally unavailable. Hence, we followed the treatment suggested by Karkoschka (1990), where he developed 2-term exponential fits using the spectrum of Saturn as a guide for modifying the room temperature measurements of methane's absorption coefficients.

2.5 Ground reflectivity

The reflectivity of the ground as a function of wavelength is somewhat constrained at the continuum wavelengths longward of about 0.5 μm, where the extinction by the overlying aerosols is not too great. Longward of 1 μm, the absolute calibration of the observations is not extremely reliable, and shortward of about 0.5 μm the overlying haze aerosols are so dark and optically thick that the observations from outside Titan's atmosphere are not strongly sensitive to the ground reflectivity. The ground albedo *vs* wavelength is somewhat constrained between these two limits once the number and refractive index of the haze particles are determined by other observations. The values we used in both of our models are shown in Fig. 2.

2.6 Radiative transfer calculations

In both of our models, we divided the atmosphere into 30 homogeneous layers. The radiative properties of each layer was obtained by a doubling code, and layer adding was used to obtain the intensities at each interface. We used 11-point Gaussian

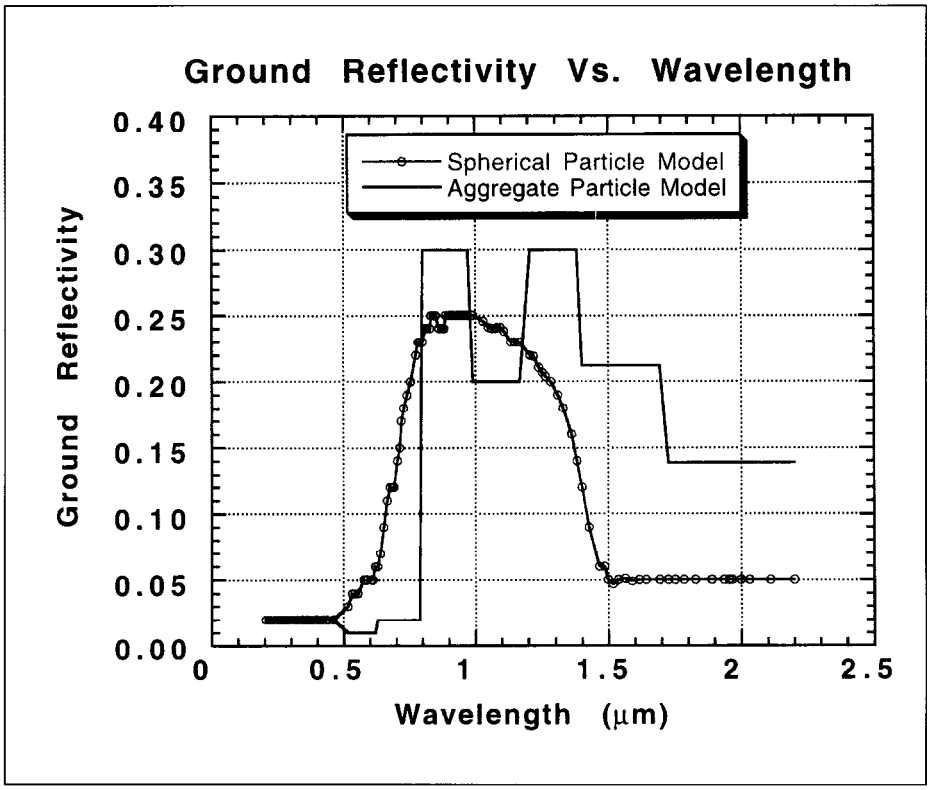

Fig. 2. The reflectivity of the ground as a function of wavelength used in the two models. Longward of 1 μm, the ground albedo depends sensitively on the small and uncertain absorption coefficient of methane in the window regions, as well as on the uncertain absolute calibration of the observations of Fink & Larson that were available when our models were computed. Shortward of about 0.5 μm, the haze aerosols are so dark and thick that observations made from outside Titan's atmosphere are not very sensitive to the ground albedo.

quadrature for the upward and downward integrations at each of 104 wavelength bins from 0.2 μm to 2.5 μm wavelength. The only wavelength-dependent quantity adjusted to make the models fit the observations was the albedo of the ground (shown in Fig. 2 for the two models). Observations from outside the atmosphere are sensitive to this quantity only at red or longer continuum wavelengths. The mass production rate was adjusted to give a reasonable fit to the methane band near 0.73 μm. The charge is adjusted to give the largest particles that can still produce the high degree of linear polarisation observed near 90° phase. This particle size turns out to give a rate of change of aerosol opacity with wavelength that permits penetration to reasonable methane abundances at longer wavelengths (0.89 μm). The level of rainout is selected to give a reasonable match to the strength of the weak methane band near 0.62 μm. Thin condensation clouds at lower altitudes are poorly constrained by the available observations, so long as their optical depth averaged over the disc is ≤ about 0.5.

2.7 Particle shape

It has been known for some time that models using only spherical particles are not able to simultaneously reproduce the high degree of linear polarisation and the strong degree of forward scattering observed for Titan (Hunten et al. 1984). Recently, West & Smith (1991) have investigated the properties of particles produced by diffusion limited aggregation. Particles produced in this way are assembled by adding small individual spheres to a growing cluster. Such particles can come closer to fitting simultaneously the constraints from polarisation and forward-scattering measurements than can purely spherical particles. Nevertheless, at levels in Titan's atmosphere below the altitude range where spherical 'monomers' are being produced directly from the gas, the mechanism for growth of the aggregate particles is expected to be dominated by ballistic cluster-cluster (BCAA) aggregation rather than by aggregation of clusters with monomers.

The BCAA mechanism will produce an even more open type of particle with a smaller fractal dimension that is capable of even more forward-scattering for the same

degree of linear polarisation in a single-scattering as aggregate particles formed by addition of small 'monomers' to clusters (Lemmon, 1994). Fig. 3 shows an aggregate particle consisting of 16 small spherical particles produced by BCAA of monomers of size 0.06 μm. Fig. 4 shows the single-scattering phase function of the particle shown in Fig. 3 compared to the forward-scattering constraint from Rages & Pollack (1983). Note that the BCAA phase function can achieve the degree of forward-scattering required for Titan while simultaneously producing a very high degree of linear polarisation in a single-scattering.

2.8 Constraints

Both the spherical particle model and the newer BCAA aggregate models were constrained by comparison with key optical observations of Titan. In both cases, the

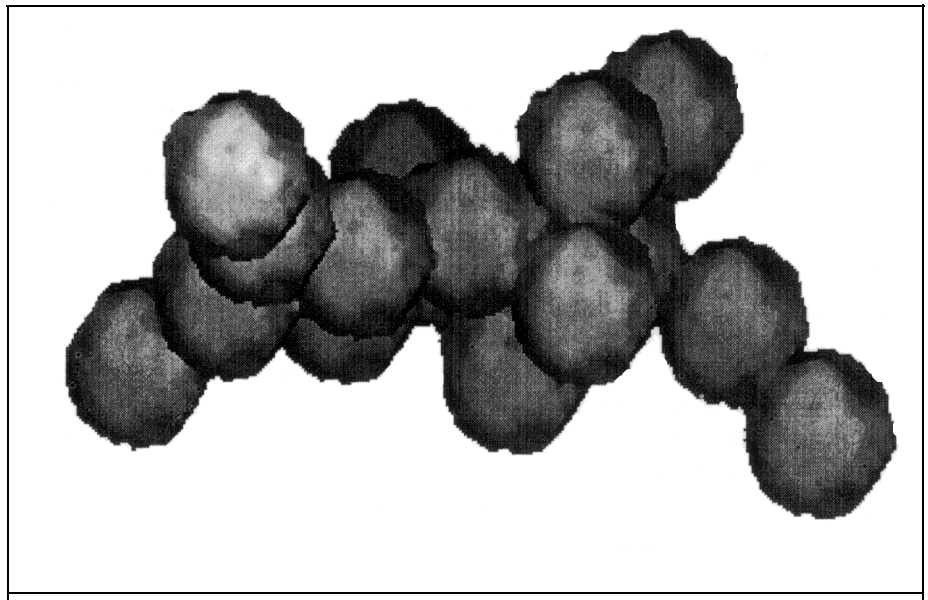

Fig. 3. Fractal aggregate picture. This is an example of an aggregate of 16 monomers. It was formed by ballistic cluster-cluster aggregation, which results in a fractal structure with a dimension of about 2.

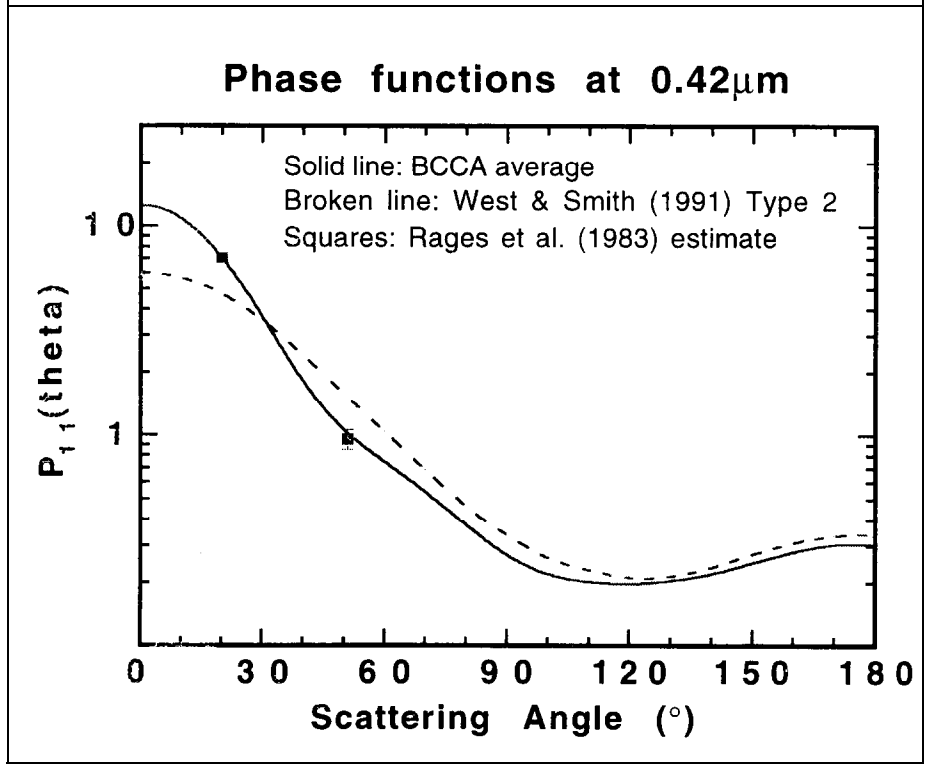

Fig. 4. Dashed line: the phase function of West & Smith (1990) for type II diffusion limited aggregate (DLA). Solid curve: the average phase function of eight Ballistic cluster-cluster aggregate particles consisting of 16 monomers each of radius 0.06 μm having the refractive indices of tholins. The constraint from Rages et al. (1983) on the ratio of the value of the single-scattering phase function at 21° scattering angle to the value at 50° is indicated by the squares. The BCAA phase function is sufficiently forward-scattering to meet this constraint, and is still capable of producing a high degree of linear polarisation, as shown in Fig. 9 below.

constraints are applied beginning with those that bear on the nature of the particles near the top of the atmosphere first, then working down through the atmosphere. The brightness in the UV and the ratios of brightness at high phase angles refer to the highest levels, and are used to constrain the mass production rate, the electrical charge on the haze aerosols and the eddy diffusion constant. These are adjusted to give aggregate particles that can produce the largest ratio of brightness at the high phase angles and still give large single-scattering linear polarisation. The brightness in the strong methane band near 0.89 μm is also sensitive to these parameters.

The brightness in the weaker methane bands in the visible is determined by the altitude at which rainout is presumed to clear the photochemical haze aerosols from the atmosphere. In the lower stratosphere and troposphere, thin clouds of particles large compared to the wavelength are added to match the observed depths of methane bands of intermediate strength (as near 0.72 μm). In the model using spherical particles, these are added in a layer between 64 km and 48 km altitude, where they are presumed to consist of stratospheric hydrocarbons that condense as they diffuse to lower and cooler altitudes, as suggested by Sagan & Thompson (1984). A second layer is assumed to exist at 12-24 km altitude, possibly consisting of condensed methane. The optical constraint placed on these cloud layers by the observed strengths of the methane bands is not strong, although it does limit the optical depth of these clouds averaged over the disc to be no greater than a few tenths. In the spherical model, both layers are assumed to have an optical depth of 0.1. In view of the weak nature of this constraint, in the aggregate model we assumed these condensation clouds have an optical thickness of 0.5 and that they are uniformly distributed between the surface and the altitude of 'rainout' (below which the small haze particles are removed).

At the bottom of the model, the surface is treated as a Lambert surface with a wavelength dependent reflectivity. The value of the surface reflectivity depends on the strength of the weak methane absorption in windows between the strong methane absorption bands in the near-IR, and so is somewhat uncertain. We used somewhat different values of surface reflectivity in our aggregate and spherical models, as shown in Fig. 2.

3.1 Model parameters

A relatively small number of free parameters (*MPR*, *Q*, rainout altitude *Z*) were tuned to fit the constraints imposed by polarisation, geometric albedo and the large amount of forward-scattering (aggregate model only). The value of the eddy diffusion was also weakly constrained by the aggregate model. The parameters of the best fitting models of both type are summarised in Table 1.

The vertical distributions of the haze particles in both the spherical particle and aggregate particle models are shown in Fig. 5 (for particle size), Fig. 6 (for column mass density) and Fig. 7 (for geometric cross section).

Both models fit the geometric albedo and polarisation constraints quite well (see Figs. 8 and 9). The aggregate model also fits the forward-scattering constraint reasonably well. Note that no vertical motions have been assumed in the model to suspend larger particles above smaller ones. Dynamical effects still remain to be added to aggregate particle models. Models using spheres cannot fit the forward-scattering constraint while fitting the polarisation constraint without invoking dynamical effects to suspend a thin layer of larger particles near the top of the atmosphere (Toon et al., 1992).

3.2 Solar flux profiles

Undoubtedly, considerable further refinement of such models will be done as the data set available for constraining them grows. For example, spectra in the near-IR are

3. Results for Models using Spherical Particles and Aggregate Particles

Table 1. Parameters of spherical particle and aggregate models.

Parameters	*Spherical model*	*Aggregate model*
Mass production rate, *MPR*	4×10^{-15} g/cm^2/s @ 350 km	15.5×10^{-15} g/cm^2/s @ 250 km
Eddy diffusion, *K*	(Various values permitted)	0.15 × Yung et al., 1984 (as modified by Toon et al., 1992)
Aerosol shape	Spherical	Cluster cluster aggregates
Aerosol density	1 g/cm^3	Same
Charging, *Q*	30e$^-$/μm particle radius	26e$^-$/μm particle radius
Rain out below altitude *Z*	56 km	88 km
Total aerosol mass (column)	280 mg/m^2	220 mg/m^2
Real refractive index of haze, n_r	tholin (Khare et al., 1984)	Same
Imaginary refractive index of haze, n_i (see Fig. 1)	Within ~20% of tholin (Khare et al., 1984)	4/3 × tholin
Temperature-pressure profile	Coustenis, pers. comm.	Coustenis, pers. comm., 1993
Methane mixing ratio	1.8% (stratosphere) 4.4% (surface)	Same
Methane absorption shortward of 1 μm	2-term exponential fits following Karkoschka (1990)	Same
Methane absorption longward of 1 μm	8-term exponential sum fit to band model extrapolation of cold laboratory measurements of Giver et al. (1990)	Same
Condensation cloud optical thickness and location	τ = 0.1 (~55 km) τ = 0.1 (~20 km)	τ = 0.46, uniformly distributed below rainout
Condensation cloud optical parameters	g1=0.62, g2=-0.294, f1=0.763, w=1.0	Same
Surface Reflectivity, $R(\lambda)$	(See Fig. 2)	(See Fig. 2)

becoming available at different phases in Titan's orbit and with improved absolute calibration (see Lemmon et al., 1995). Observations with increasing spatial resolution are also becoming available (Smith et al., 1996). Nevertheless, at the time the Huygens instruments were being designed, the models shown here were used to estimate the penetration of solar flux into Titan's atmosphere. The difference in the penetration of sunlight in the two models may give some idea of the level of uncertainty in the existing models.

Fig. 11 shows the spectrum of downward solar flux (direct flux plus the diffuse flux) at several altitudes in Titan's atmosphere from the aggregate model. The upward flux is shown in Fig. 12. The cumulative distribution of the net (total downward minus upward) solar flux is shown at several altitudes in Fig. 13. Note that the DISR instrument, which covers the range from 0.35 μm to just beyond 1.62 μm, directly measures some 88% of the net solar flux at 160 km altitude, and 90% or more of the net flux at altitudes below about 100 km.

Fig. 14 shows measured downward diffuse and direct solar fluxes in the 0.2-2.5 μm band for the aggregate and spherical models at a solar zenith angle of 50°. Fig. 15 shows the upward and net solar fluxes in this band for the two models at the same location. Note that the net fluxes in the two models do not converge to the same values at the top of the atmosphere at this solar zenith angle. While both models have been constrained to fit the observed geometric albedo spectrum at small phase angles, the different amounts of forward-scattering in the two models gives a different penetration of solar energy at other locations.

Also, since the two models have the same surface properties, the fluxes are about

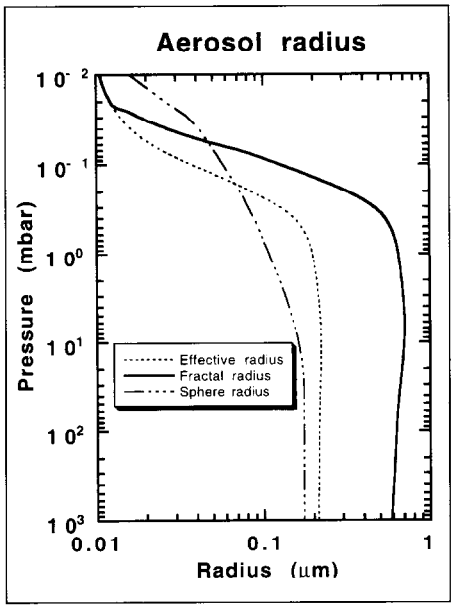

Fig. 5. Aerosol size. The heavy solid line shows aerosol fractal radius (approximately the radius of gyration) as a function of altitude. The dashed line shows the radius of an equal volume sphere corresponding to the aggregate particles. The dotted and dashed line shows the variation of mean radius of haze particles in the spherical particle model as a function of altitude for comparison.

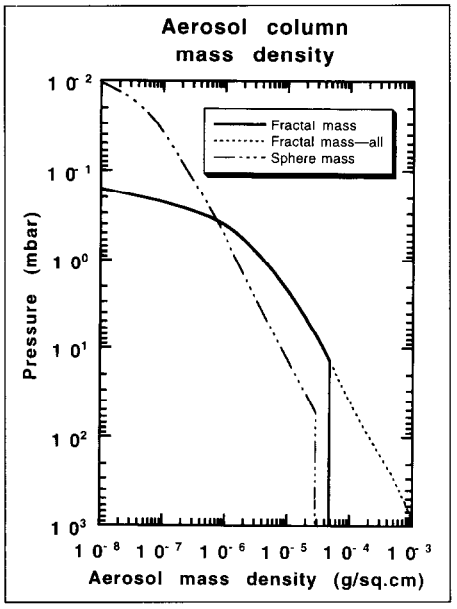

Fig. 6. Column mass density. The solid line is the cumulative mass as a function of increasing pressure for the aggregate model, including the break near 10 mbar due to rainout below. The dotted and dashed line is the corresponding curve for the spherical model. The dashed line shows the column mass density for the case of no rainout in the aggregate model.

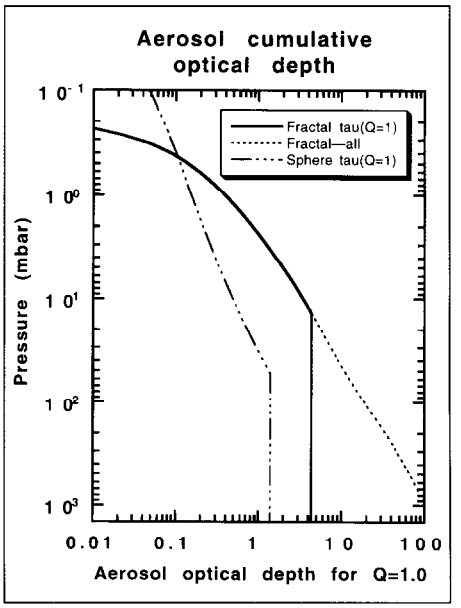

Fig. 7. At each wavelength, the actual cross section for scattering is the product of the geometric cross-section and the efficiency factor, $q(\lambda)$, which varies from several tenths to several. Thus, the optical depth varies significantly with wavelength. If q is arbitrarily set to unity, the aerosol optical depth due to the geometric cross-section alone gives some indication of the vertical distribution of optical depth in each model. The solid line shows the column integrated geometric cross-section for the aggregate model. The dotted and dashed curve shows the same parameter for the spherical particle model. The dotted line shows the curve for the aggregate model without rainout.

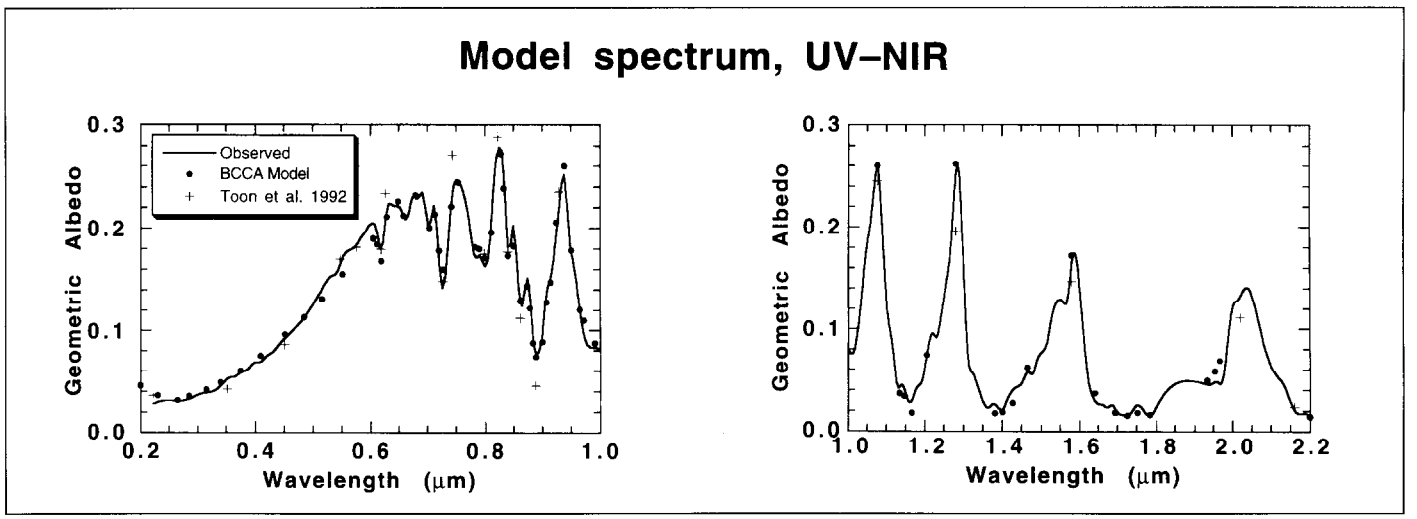

Fig. 8. Model albedo. The observed albedo (solid line) from Courtin et al. (1991), Neff et al. (1984) and Fink & Larson (1979) is compared with the aggregate model albedo (solid circles) and the Toon et al. (1992) model albedo (+).

the same in the two models at low altitudes. DISR will be able to obtain images with good signal-to-noise ratios near the surface in both models with integration times of a few tens of milliseconds. The levels of downward diffuse flux show a break in slope at the altitudes of rainout in the two models, near 88 km in the aggregate models and near 56 km in the spherical particle model. Note that the more forward-scattering nature of the aggregate model carries more of the downward flux in the diffuse flux and less in the direct flux. Also, the upward flux is somewhat higher in the spherical particle model than in the aggregate model above the rainout altitude. On the whole, at 50° solar zenith angle, solar energy is deposited somewhat less deeply in the aggregate model than in the spherical model in the photochemical haze region. Below the altitudes of rainout, both models deposit the solar energy in similar manners, as shown by the overlap of the net flux profiles.

It will be interesting to see the extent to which direct measurements by the Huygens instruments are similar to these early models of the penetration of solar radiation into Titan's atmosphere.

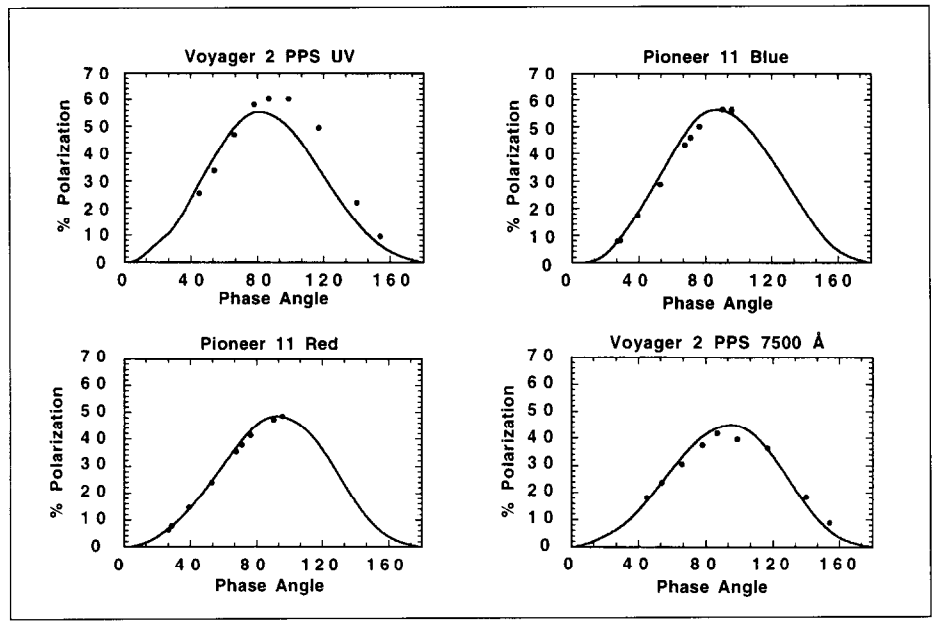

Fig. 9. Polarisation of the aggregate model (filled circles) compared with observed polarisation (solid lines) at four wavelengths. The Pioneer observations are from Tomasko & Smith (1982); the Voyager observations are from West et al. (1983).

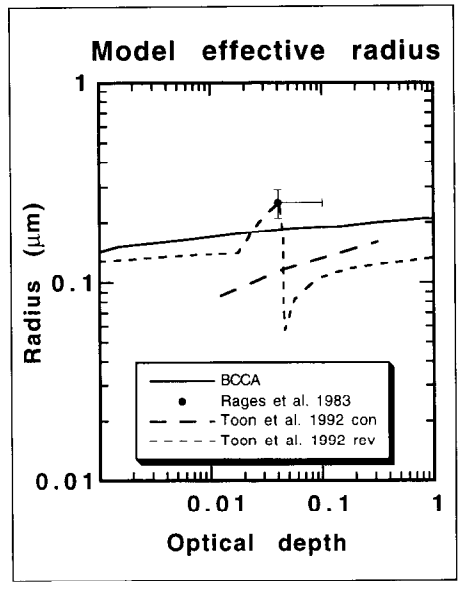

Fig. 10. Aerosol effective radius as a function of altitude. The aerosol effective radius is compared with the measurements of Rages et al. (1983) and the models using spherical particles by Toon et al. (1992) (long-dash) and revised (short-dash) models. For the Toon et al. (1992) models, the effective radius is that of a log-normal distribution of spheres. For the fractal model, the effective radius is the radius of a sphere that has the same forward-scattering properties as all of the fractal particles at a given altitude. The structure is due to a vertical wind that causes a detached haze layer. Note that the Rages et al. (1983) observations pertain to the main (lower) haze layer.

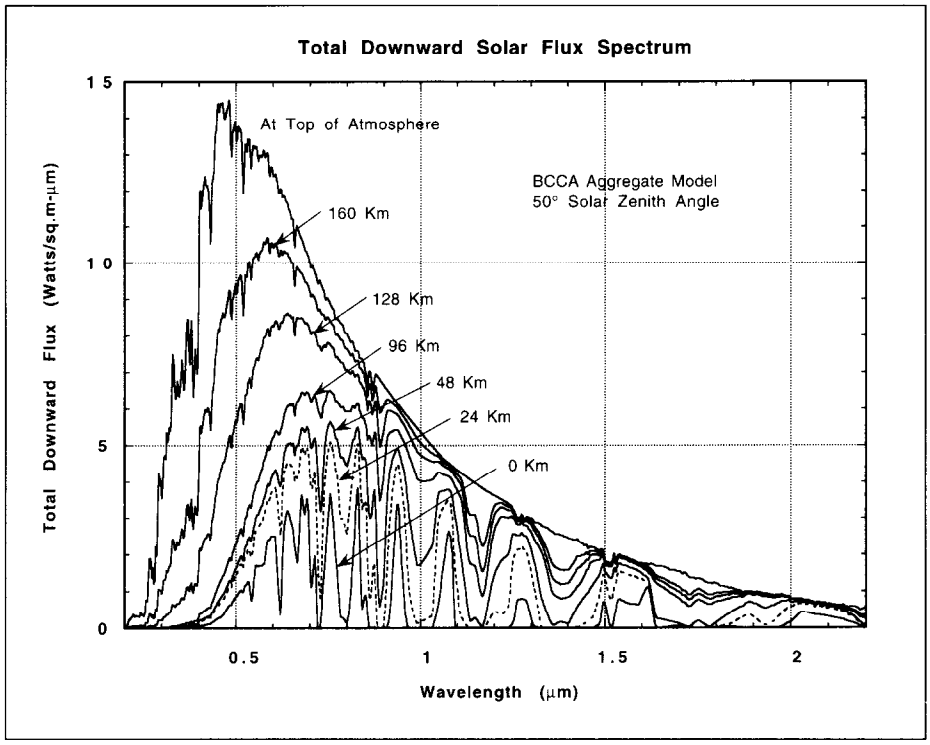

Fig. 11. Spectrum of the total downward (direct plus diffuse) flux at several altitudes in the aggregate model at a solar zenith angle of 50°.

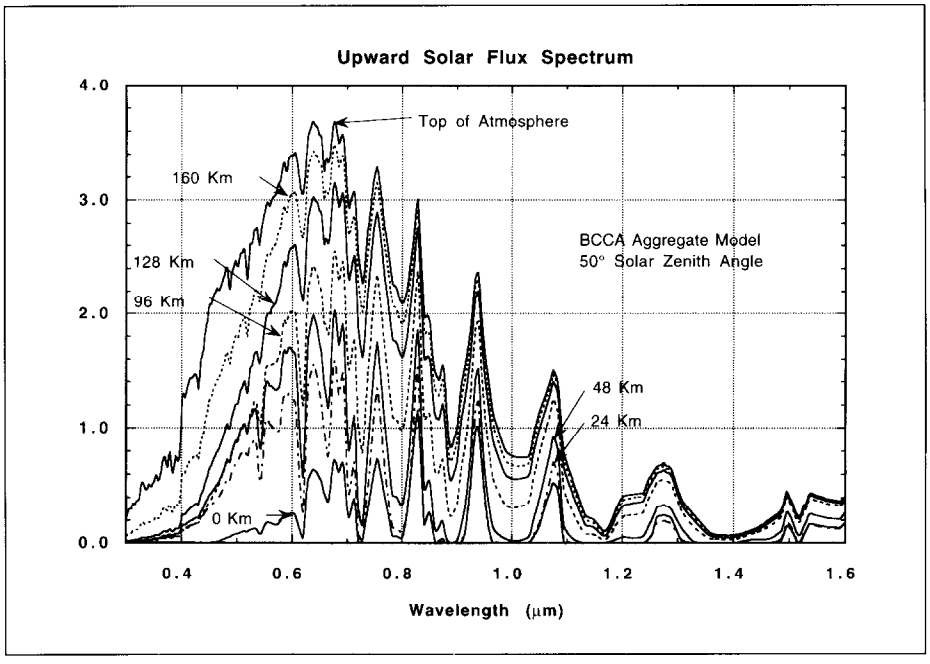

Fig. 12. Spectrum of the upward solar flux at several altitudes in the aggregate model at a solar zenith angle of 50°.

Fig. 13. Cumulative distribution of net solar net flus versus wavelength at several altitudes for the aggregate model. Note that DISR measurements, covering the 0.35-1.7 μm spectral range, include all but about 12% of the solar net flux deposited below altitudes of 160 km.

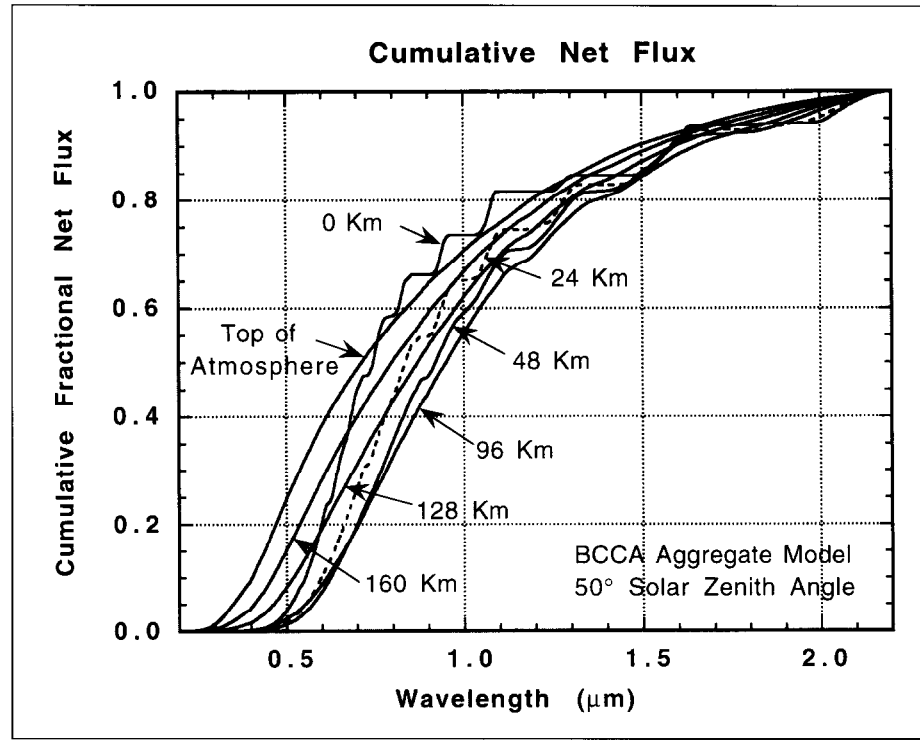

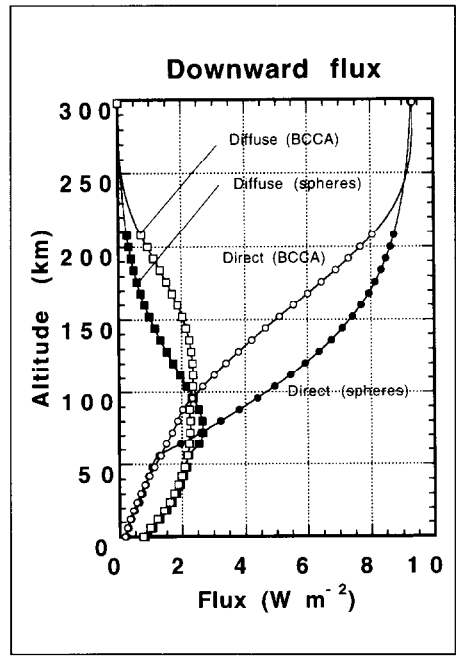

Fig. 14. Downward direct and diffuse fluxes in the 0.2-2.2 μm spectral range versus altitude at a location where the local solar zenith angle is 50° for the aggregate model and for the model using spherical particles.

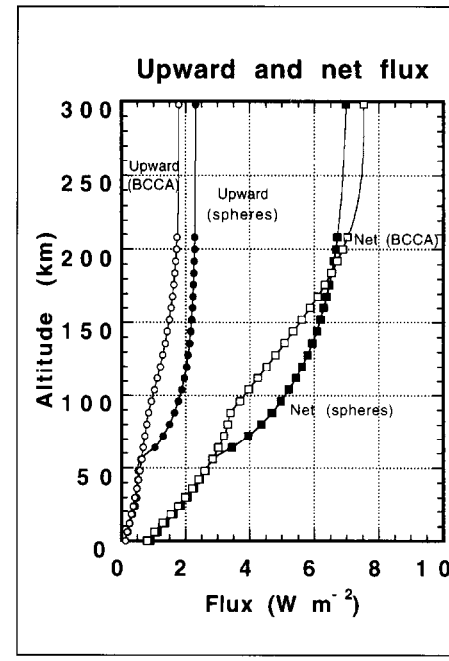

Fig. 15. As Fig. 14 but for the upward and net solar fluxes.

References

Asano, S. & Uchiyama, A. (1987). Application of an extended ESFT method to calculation of solar heating rates by water vapor absorption. *J. Quant. Radiat. Transfer* **38**, 147-158.

Courtin, R., Wagener, R., McKay, C. P., Caldwell, J., Fricke, K.-H., Raulin, P. & Bruston, P. (1991). UV spectroscopy of Titan's atmosphere, planetary organic chemistry and prebiological synthesis. *Icarus* **90**, 43-56.

Fink, U. & Larson, H. P. (1979). The infrared spectra of Uranus, Neptune, and Titan from 0.8 to 2.5 μm. *Astrophys. J.* **233**, 1021-1040.

Giver, L. P., Benner, D. C., Tomasko, M. G., Fink, U. & Kerola, D. (1990). Gaussian quadrature exponential sum modeling of near infrared methane laboratory spectra obtained at temperatures from 106 to 297 K. In *First International Conference on Laboratory Research for Planetary Atmospheres*, 147-156.

Hunten, D. M., Tomasko, M. G., Flasar, F. M., Samuelson, R. E., Strobel, D. F. & Stevenson, D. J. (1984). Titan. In *Saturn* (Eds. T. Gehrels & M. S. Matthews), Univ. of Arizona Press, pp671-759.

Karkoschka, E. (1990). Saturn's atmosphere in the visible and near-infrared: 1986-1989. Ph.D. Dissertation, Department of Planetary Sciences, University of Arizona, Tucson, Arizona, USA.

Khare, B. N., Sagan, C., Arakawa, E. T., Suits, F., Callicott, T. A. & Willaims, M. W. (1984). Optical constants of organic tholins produced in a simulated Titanian atmosphere: From soft X-rays to microwave frequencies. *Icarus* **60**, 127-137.

Lemmon, M. T. (1994). Observations and Models of Titan. Ph.D. Dissertation, Department of Planetary Sciences, University of Arizona, Tucson, Arizona, USA.

Lemmon, M. T., Karkoschka, E. & Tomasko, M. G. (1995). Titan's rotational light-curve. *Icarus* **113**, 27-38.

Neff, J. S., Humm, D. C., Bergstralh, J. T., Cochran, A. L., Cochran, W. C., Barker, E. S. & Tull, R. G. (1984). Absolute spectrophotometry of Titan, Uranus, and Neptune: 3500-10500 Å. *Icarus* **60**, 221-235.

Rages, K. & Pollack, J. B. (1983). Vertical distributions of scattering hazes in Titan's upper atmosphere. *Icarus* **55**, 50-62.

Rages, K. & Pollack, J. B. (1980). Titan aerosols: Optical properties and vertical distribution. *Icarus* **41**, 119-130.

Sagan, C. & Thompson, W. R. (1984). Production and condensation of organic gases in the atmosphere of Titan. *Icarus* **59**, 133-161.

Smith, P. H., Lemmon, M. T., Lorenz, R. D., Sromovsky, L. A., Caldwell, J. J. & Allison, M. D. (1996). Titan's Surface, revealed by HST imaging. *Icarus* **119**, 336-349.

Tomasko, M. G., Pope, S., Kerola, D., Smith, P. & Giver, L. (1989). Constraints on haze and cloud structure from Titan's albedo between 1 and 2.5 μm. *Bull. Am. Astron. Soc.* **21**, 961.

Tomasko, M. G. & Smith, P. H. (1982). Photometry and polarimetry of Titan: Pioneer 11 observations and their implications for aerosol properties. *Icarus* **51**, 65-95.

Toon, O. B., McKay, C. P., Griffith, C. A. & Turco, R. P. (1992). A physical model of Titan's aerosols. *Icarus* **95**, 24-53.

Toon, O. B., Turco, R. P. & Pollack, J. B. (1980). A physical model of Titan's cloud. *Icarus* **43**, 260-282.

West, R. & Smith, P. H. (1991). Evidence for aggregate particles in the atmospheres of Titan and Jupiter. *Icarus* **90**, 330-333.

West, R. A. (1991). Optical properties of aggregate particles whose outer diameter is comparable to the wavelength. *Applied Optics* **30**, 5316-5324.

West, R. A., Lane, A. L., Hart, H., Simmons, K. E., Hord, C. W., Coffen, D. L., Esposito, L. W., Sato, M. & Pomphrey, R. B. (1983). Voyager 2 photopolarimeter observations of Titan. *J. Geophys. Res.* **88**, 8699-8708.

Yung, Y. L., Allen, M. & Pinto, J. P. (1984). Photochemistry of the atmosphere of Titan: Comparison between model and observations. *Astrophys. J. Suppl. Ser.* **55**, 465-506.